

MOF-Derived Onion-Like Carbon with Superior Surface Area and Porosity for High Performance Lithium-Ion Capacitors

Antonius Dimas Chandra Permana,^[a] Ahmad Omar,^{*[a]}
 Ignacio Guillermo Gonzalez-Martinez,^[a] Steffen Oswald,^[a] Lars Giebelner,^[a]
 Kornelius Nielsch,^[b, c] and Daria Mikhailova^{*[a]}

Lithium-ion capacitors (LICs), potentially bring together the advantages of batteries and supercapacitors. For the faradaic anodes, nanostructured carbonaceous materials hold immense potential, in contrast to graphite where limitations in Li-ion diffusivity exist. Herein, onion-like carbons (OLCs), synthesized from Fe-BTC metal-organic framework (MOF), is implemented as the LIC anode, owing to its high charge storage capacity and rate capability as compared to graphite. The enhanced charge storage and Li-ion transference in OLCs was understood to be

due to hierarchical porosity with accessible inner voids along with high defect concentration. Therefore, full-LIC cells with OLC anodes exhibited a markedly higher specific capacitance and an enhanced rate capability than graphite-LIC. The OLC-LIC achieved an outstanding maximum energy density of 224 Wh kg^{-1} at 122 W kg^{-1} and maximum power density of 14436 W kg^{-1} at 80 Wh kg^{-1} . Thus, MOF-derived OLC with distinctive morphology is presented as a highly attractive anode for practical LIC systems.

Introduction

In the last decades, there has been a rapid development of energy storage systems for hybrid electric vehicles, mainly focusing on Li-ion battery (LIB) and supercapacitor technology. On one hand, LIBs boast of high energy density through the bulk interaction with Li involving different mechanisms. In contrast, supercapacitors, utilizing electrochemical double layer capacitance, allow for ultrafast charge and discharge demonstrating high power density. Hybrid asymmetric supercapacitor or often referred to as a Li-ion capacitor (LIC) is a relatively newer concept which aims to incorporate the advantages of LIBs in a supercapacitor system. In a LIC, the cathode is an

electrochemical double-layer capacitor, but a conventional LIB electrode is used as an anode.^[1] The anode is pre-lithiated, i.e., the Li ions are initially stored via a Faradaic process. During subsequent operation as a full-cell supercapacitor system, the stored Li ions at the anode act as an additional Li source. In particular, the LIB anode allows for higher charge storage whereas the supercapacitor ensures fast charge-discharge characteristics with long cycle life, enabling simultaneous improvement in both the energy and power densities. Furthermore, comparable to $2.5 \text{ V} \leq U \leq 4.2 \text{ V}$ potential range of LIBs, LICs offer a higher potential range of $2.2 \text{ V} \leq U \leq 3.8 \text{ V}$,^[2] in comparison to supercapacitors, which commonly have a potential limitation of $2.5 \text{ V} \leq U \leq 2.7 \text{ V}$ due to degradation phenomena at $U > 2.8 \text{ V}$.^[3,4]

The anode for LIC systems, which achieves higher charge storage, needs to match well with the high current rate performance of the double-layer capacitor cathode. Therefore, the anode choice becomes key towards superior LIC performance. Although a wide variety of high-rate capable LIB anodes are, in principle, available, carbonaceous materials are particularly advantageous for high energy and power densities as well as offer potential benefits with regards to cost and environmental concerns, and have therefore been actively explored for LIC applications. Logically, graphite is a very well established LIB anode, with a low lithiation potential of close to 0 V vs. Li/Li^+ , a relatively high theoretical capacity (372 mAh g^{-1}) and shows high cycling reversibility.^[5] Unfortunately, graphite has limitations with regards to Li-ion diffusivity during the intercalation/de-intercalation process, significantly affecting their high rate performance leading to low practical specific capacities.^[5] Additionally, under high currents, lithium

[a] A. Dimas Chandra Permana, Dr. A. Omar, Dr. I. Guillermo Gonzalez-Martinez, Dr. S. Oswald, Dr. L. Giebelner, Dr. D. Mikhailova
 Institute for Complex Materials
 Leibniz Institute for Solid State and Materials Research (IFW) Dresden
 Helmholtzstraße 20, 01069 Dresden, Germany
 E-mail: a.omar@ifw-dresden.de
 d.mikhailova@ifw-dresden.de

[b] Prof. K. Nielsch
 Institute for Metallic Materials
 Leibniz Institute for Solid State and Materials Research (IFW) Dresden
 Helmholtzstraße 20, 01069 Dresden, Germany

[c] Prof. K. Nielsch
 Institute for Materials Science
 Technische Universität Dresden
 Helmholtzstraße 7a, 01069 Dresden, Germany

 Supporting information for this article is available on the WWW under <https://doi.org/10.1002/batt.202100353>

 © 2022 The Authors. *Batteries & Supercaps* published by Wiley-VCH GmbH. This is an open access article under the terms of the Creative Commons Attribution Non-Commercial NoDerivs License, which permits use and distribution in any medium, provided the original work is properly cited, the use is non-commercial and no modifications or adaptations are made.

plating along with dendritic growth on the graphite surface have been reported,^[6] which aggravates the safety issue.

Therefore, addressing the shortcomings in Li-ion diffusivity and specific capacity of graphitic anodes at high rates, especially required for LIC application, has been an active research focus.^[7] For this purpose, strategies involve mainly either developing active sites through either enlarging the specific surface area e.g. by creating more pores and channels for lithium intercalation,^[8] or increasing the defect density e.g. through higher edge density.^[9] In this regard, a novel carbon allotrope called onion-like carbons (OLC) may be quite suitable. OLC or carbon nano-onions consist of concentric graphitic shells and can also be understood as large multi-layered fullerenes in an ideal case.^[10,11] Practically, OLCs have polyhedral, defect-rich shells, and depending on the synthesis procedure, they may have a hollow or a solid core.^[12] The size of the outermost shell lies in the range of 3–100 nm. The unique structure of OLCs offers large surface area and high electrical conductivity, along with high defect concentration in the graphitic structure.^[12] As a result, OLCs have been actively explored in the field of energy storage, as conductive additives or electrodes for supercapacitors and LIBs,^[12] as well as active materials for photovoltaic cells^[13–16] and H₂ storage devices.^[17] Moreover, depending on the synthesis procedure and processing, OLCs display a large variety in surface area and defect content.^[12] Not only they can be doped with N in the lattice, but also the outer surface can be functionalized. Hence, they are quite promising for LIC technology where a balance of different aspects is sought for.

As mentioned, the structure and morphology of the OLCs strongly depend on the synthesis procedure. The most common synthesis route via nanodiamond annealing produces OLCs with smaller surface areas (<600 m² g⁻¹).^[12] The shells are highly graphitic in nature such that they predominantly show good capacitive behavior.^[18] Recently, Presser's group has utilized nanodiamond-OLCs as templates for metal oxides hybrids towards improved LIC performance.^[19–21] Alternatively, arc-discharge method, although results in OLCs with very high surface area (>900 m² g⁻¹),^[22] produces OLCs as one of the many by-products,^[23] and significant steps are needed to obtain a high purity. Other synthesis routes for OLCs have been explored in literature such as carbonization of natural raw/waste materials, where the produced OLCs have been explored for supercapacitors.^[24] There are only a few reports using this route towards hybrid capacitors but they report relatively small surface areas (~140 m² g⁻¹^[25] and ~50 m² g⁻¹^[26]), and the synthesis process offers limited scope of controlling the morphology.

In the past years, porous carbons derived from metal-organic frameworks (MOFs) have been quite promising towards supercapacitor applications as the MOF-preursors imbue highly desirable nanostructured porosity.^[27,28] Recently, synthesis of OLCs has been demonstrated by a direct MOF-pyrolysis.^[29] This method can produce OLCs with high surface area (>800 m² g⁻¹), which do not need further physical/chemical activation.^[30] More importantly, MOF-route involves a simple annealing process leading to ease in control of system

atmosphere and pressure, as well as allows for control of structural parameters and dopants, thereby enabling greater control over structure and morphology. Therefore, MOFs-derived OLCs have significant potential for direct implementation as anodes in LIC system. Additionally, with increasing commercialization of a wide variety of MOFs, synthesis of OLCs via MOF-route offers low-cost, easy scalability, high purity and simpler equipment setup, making it economically viable for industrial application.

The present work focuses on the implementation of OLCs with specialized morphology as anodes towards LIC technology along with commercial graphite KS6L for comparison. The OLCs are synthesized using an existing MOF-pyrolysis route^[29] which imbues a high surface area and porosity along with accessible inner voids. Both OLC and graphite electrode materials are tested in half-cell setup (vs. lithium) as well as in full-LIC cells with commercial activated carbon YP50F as the cathode. Full-cell LIC with OLC as anode exhibited an outstanding 224 Wh kg⁻¹ energy density at 122 W kg⁻¹ power density and excellent 14436 W kg⁻¹ power density at 80 Wh kg⁻¹ energy density. Thus, OLCs prepared though the MOF-precursor route, are a highly attractive anode material for practical LICs.

Results and Discussion

The OLC material was prepared by the pyrolysis of the commercial Fe-based MOF, Basolite F300, resulting in high surface area OLCs, as reported previously.^[29] Subsequently, detailed morphological, structural and physical characterization was performed on the as-synthesized OLC along with the commercial graphite KS6L (henceforth only referred to as graphite) for comparison. Commercial activated carbon YP50F (henceforth only referred to as activated carbon, or AC), chosen as the cathode for full-cell LIC, has a very large surface area along with high graphitic nature, and therefore was also included in the characterization for comparison.

The morphology of the graphite and the as-produced OLC is investigated by SEM, as shown in Figure 1a and 1b. As expected, for graphite, plate-like particles were observed that coincides with typical descriptions in literature.^[31] For as-prepared OLCs, agglomerates of mainly spherical particles were visualized, with the absence of any other carbon nanostructure such as carbon nanotubes or nanofibers (Figure 1b). In contrast, flat surfaces were observed for AC (Figure S1a, Supporting Information). TEM images of the OLC sample show a mostly shell-like structure, with small amounts of amorphous carbon (Figure S1b). HR-TEM investigation on the as-synthesized OLC material, shown in Figure 1(c), confirms the presence of onion-like carbon structures with multiple fullerene-like layers. 10–20 graphitic layers are seen in the OLCs. The interplanar distances (*d*-spacing) between graphitic layers from the onion shells were found to have an average value of 0.38 nm. The value is similar to what has been reported earlier,^[29] although slightly larger than the known interlayer distance in graphite (0.34 nm).^[32] Noticeably, diffused graphitic structure was observed at the point of curvatures/bends, suggesting a higher defect density

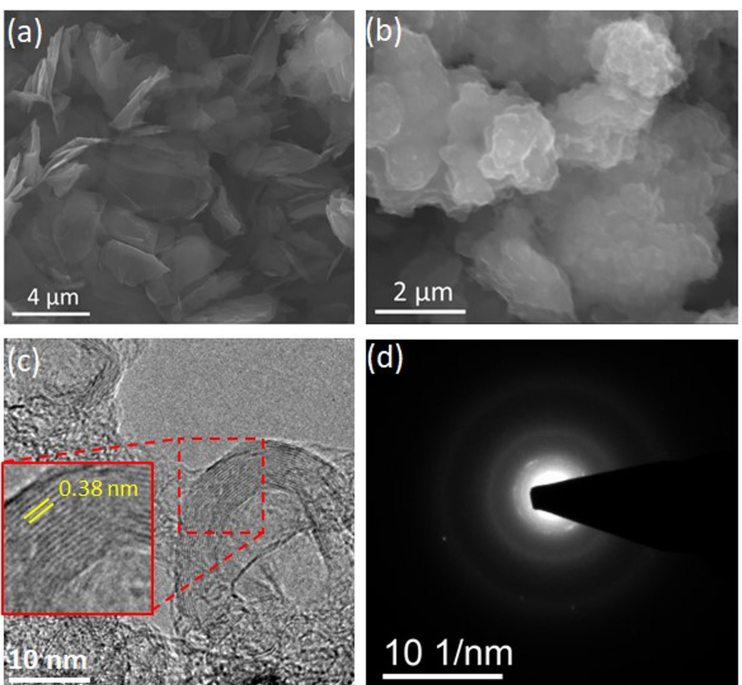


Figure 1. SEM images (SE detector) of a) graphite and b) OLC; c) HR-TEM image of OLC and d) the corresponding SAED pattern.

in those regions (Figure 1c). The corresponding selected area electron diffraction (SAED) pattern in Figure 1d shows mostly diffused rings, suggesting an absence of pronounced long-range order. Although a few diffraction spots can be seen, they are rather stretched instead of sharp intensities, pointing to a defect-rich nature of the OLCs. The defect-rich nature is likely a result of the low-crystallinity MOF used as precursor as well as the lower temperature synthesis of OLCs as compared to conventional high temperature syntheses from nanodiamonds, arc-discharge route etc.^[12]

Figure 2a shows the X-ray diffraction (XRD) patterns for graphite and OLC along with that of Basolite F300 MOF. Graphite showed sharp reflections, which were indexed with hexagonal $P6_3/mmc$ structure (space group no. 194)^[33] along with a possible small fraction of trigonal $R\bar{3}m$ (space group no. 166).^[34] On the other hand, no reflections were observed for

OLC sample. Given the nanoscale structure of the OLC, since only a few graphitic layers are present, the graphitic peaks should be significantly broadened. Absence of sharp diffraction signals in carbon nanomaterials with spherical morphology has been well reported.^[35,36] Coupled with the defect-rich nature as mentioned in the TEM discussion earlier, broadening in the XRD data for OLC is expected to be rather severe. Therefore, there is an absence of a perceivable graphitic reflection in the XRD data as observed, and is similar to what has been reported.^[29] No Basolite F300 peaks are observed in the OLC sample, suggesting complete conversion of the precursor.

Raman spectroscopy was conducted to understand the nature of carbon structure in OLC. Figure 2b shows the Raman spectra for graphite, OLC and AC. All of the samples exhibit a strong G-band signal which is associated with graphitic layers. The G band of graphite is observed at 1575 cm^{-1} and is quite

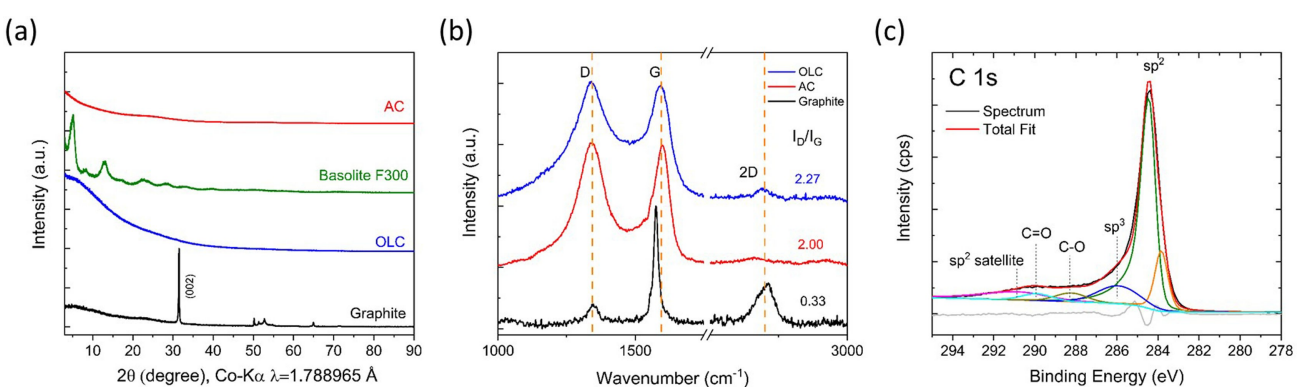


Figure 2. a) XRD patterns of graphite, OLC and Basolite F300, normalized and plotted with an offset. b) Raman spectra of graphite, OLC, and AC. c) High-resolution C 1s spectrum for OLC with fitting.

sharp whereas, for OLC and AC, the signals are rather broad and slightly shifted to a higher wavenumber at 1595 cm^{-1} . Additionally, strong D-band signals, attributed to disordered carbon and defects in the graphitic structure, are observed for OLC and AC at 1340 cm^{-1} . The same is also reflected in the ratio of the integrated intensity of the D- and G-Mode signals, the I_D/I_G ratio, representing the graphitization degree in the material. Both OLC and activated carbon have I_D/I_G ratios of 2.27 and 2.00, respectively, associated with a significantly larger fraction of disordered regions than graphite, which has an I_D/I_G ratio of 0.33. In addition to disordered carbon as a secondary phase, as seen in TEM, the disordered contribution in OLC is mainly due to the defected structure at the curvature of the shells, which is in contrast to activated carbon, where it is reported to have high quantity of disordered microcrystalline edges.^[37]

A larger disordered fraction is reported to be one of the major contributions towards the broad G band.^[38–40] The disorder/defects may also lead to presence of single bonds (carbon sp³).^[41] The 2D band at 2707 cm^{-1} , particularly seen in graphite, is associated with higher order vibrational processes in graphitic layers especially in graphene.^[42] A weaker 2D band intensity or its absence, such as that observed for OLC and AC, is understood in literature to be due to presence of a mixture of sp²-sp³ hybridization along with amorphous carbon.^[43] Therefore, in accordance with the results from HR-TEM, there is likely a considerable fraction of sp³ carbon present in the material.

XPS measurements were performed on the OLC sample and an exemplary survey spectrum is given in Figure S2a in the Supporting Information. Table S1 contains the elemental analysis from XPS, confirming the high purity of the prepared sample. Apart from 97.1 at.% carbon, presence of small amount of O (~2.3 at.%) is likely due to surface oxygen bonds as a result of air exposure. Additionally, <1 at.% Fe, residual of the MOF-precursor, as well as <1 at.% Cl, residual from the etching process, were observed. Correspondingly, weak O 1s, Fe 2p and Cl 2p signals were recorded and are given in Figure S2b–d. Detailed fitting of high-resolution C 1s spectrum was performed to evaluate the carbon hybridization and is shown in Figure 2c, while the fit summary is given in Table S2. The sp² band (284.5 eV along with satellite at 290.8 eV) was defined based on the fitting of highly-ordered pyrolytic graphite (HOPG) as reference (Figure S2e). In the case of OLC, additional sp³ band was observed at 285.9 eV , in agreement with the Raman measurements. Considering the integrated area of only the main sp² and sp³ bands (Table S2), ~16% sp³ content is evaluated in the sample. C–O (288.2 eV) and C=O (290.8 eV) contributions at higher binding energies were also observed. The existence of those oxygen-containing species is supported by the oxygen spectrum with a contribution at about 532.5 eV (Figure S2b). In the case of HOPG, the signal from sp³ hybridized species or C–O/C=O bands were either absent or negligible, since the sample was cleaned and transferred under Ar.

In the case of the OLC, an additional low binding energy (BE) band contribution, centered at around 283.8 eV , is observed. Although carbide carbon is commonly expected at

binding energies below 283 eV ,^[44] according to literature, a binding energy range of 283 – 284 eV is reported for Fe_3C ^[45–47] or Fe_xC -like carbon.^[48,49] The carbonization process at 800°C may allow for formation of similar Fe_3C or Fe-rich Fe_xC species. Tian et al.^[50] similarly reported on the formation of crystalline Fe_3C nanoparticles encapsulated with graphitic-shells through a pyrolysis process at 800°C , where the corresponding BE contribution in the C 1s spectrum is fitted at 284 eV . In accordance, in the $2p_{3/2}$ part of the respective Fe 2p spectrum (Figure S2c), major BE contribution is seen around 712 eV ,^[49,50] and only a small contribution of metallic Fe^0 at around 707 eV .^[44] Nevertheless, both ICP-OES and XPS elemental analysis evaluate a trace-level iron content (<0.3 at.%). Most likely, as carried out in our case, the additional etching and washing step is not able to access and remove the small amount of such Fe species which are completely encapsulated by carbon. Therefore, even if crystalline stoichiometric Fe_3C is formed, no corresponding observation with XRD is expected as the concentration is below the detection limit (*vide supra* Figure 2a).

The BET method was used to evaluate N_2 physisorption isotherms (Figure S3a, c, e) and to conclude on the porosity and the specific surface area of the graphite, the OLC and the AC samples (Figure S3b, d, f). For all three materials, the surface area and pore volume details were evaluated from N_2 physisorption measurements using QSDFT and are summarized in Table 1. For graphite (Figure S3a), a small specific surface area of $19\text{ m}^2\text{ g}^{-1}$ along with a small total pore volume of $0.05\text{ cm}^3\text{ g}^{-1}$ were determined. The isotherm shape shows an almost reversible Type II characteristics with a narrow hysteresis over the entire p/p_0 range, as expected for a macroporous or even nonporous solid.^[51] Some micropores, ultra- and supermicropores, may also exist but are less sensitive at these measurement conditions. For the OLC material, a high surface area of $892\text{ m}^2\text{ g}^{-1}$ was calculated, which is about 50 times larger than that of graphite. Here, both inner and outer surfaces of the carbon shells are accessible.^[29,52] A very high total pore volume of $1.05\text{ cm}^3\text{ g}^{-1}$ was obtained as well, which would be advantageous for ionic transport. The surface area is higher than most of the synthesized OLC materials in literature, particularly via nanodiamond-route,^[12] as well as the recently reported routes of CVD ($464\text{ m}^2\text{ g}^{-1}$),^[53] and candle soot combustion ($50\text{ m}^2\text{ g}^{-1}$).^[26] The enhanced surface area and porosity of the OLC material can be related to the MOF precursor Basolite F300, which has a surface area of $474\text{ m}^2\text{ g}^{-1}$.^[54] As-prepared OLC sample shows a Type IVa isotherm (Figure S3c), typical for mesoporous materials.^[51] The

Table 1. Surface area and pore volume details graphite, OLC, and AC, obtained from N_2 physisorption measurements.

Sample	Specific surface area [$\text{m}^2\text{ g}^{-1}$]	Total pore volume [$\text{cm}^3\text{ g}^{-1}$]	Pore volume [$\text{cm}^3\text{ g}^{-1}$] Micropores	Meso-pores
Graphite	19	0.05	0.01	0.04
OLC	892	1.05	0.38	0.67
AC	1348	0.70	0.64	0.06

observed hysteresis loop of mainly Type H3 (a possible small mixture of Type H2(b) nature seen at high relative pressure p/p_0) with loop closure around $p/p_0 \sim 0.42$, signifies slit-like pores along with capillary or advanced condensation and a cavitation-like pore opening during desorption.^[51,52,55,56] An additional step-like feature is found in the adsorption branch at $p/p_0 > 0.9$ (marked by an arrow in Figure S3c). The additional adsorption step is discussed in literature to be an outcome of interconnected pores of different sizes, on the lines of an open-sided ink-bottle pore.^[57,58] This particularly highlights the hierarchical pore morphology with accessibility to the inner surface area of the multilayer carbon shells, where the larger mesopore inside the OLC is connected via smaller mesopores in the shells.

The AC, in comparison to graphite and OLC, showed a much larger average BET surface area of $1348 \text{ m}^2 \text{ g}^{-1}$ although with a lower total pore volume of $0.70 \text{ cm}^3 \text{ g}^{-1}$ than OLC. As per QSDFT analysis, AC mostly contains micropores in a narrow size distribution that is also expressed by the Type I isotherm (Figure S3e) along with a high N_2 uptake at $0 \leq p/p_0 \leq 0.1$, which is indicative of a microporous solid and high adsorbent-adsorptive interactions in pores with molecular dimensions.^[51] Nevertheless, a weak H4-like hysteresis was recorded in the desorption branch related to some capillary condensation in mesopores during adsorption.

Thus, the MOF-based synthesis of OLCs is indeed an effective route to prepare this particular kind of material with

superior morphology as compared to traditional synthesis techniques.

Electrochemical performance in half-cell LIB

The electrochemical performance of graphite and OLC as anodes vs. Li/Li⁺ was evaluated in a potential range of $0.01 \text{ V} \leq U \leq 3 \text{ V}$. Figure 3a and b presents the cyclic voltammetry (CV) profiles for the first 4 cycles at a scan rate of 0.2 mV s^{-1} . The CV measurements for graphite (Figure 3a) shows sharp redox peaks observed at 0.16 V during the anodic and at 0.32 V during the cathodic sweep, which is characteristic for the lithium intercalation/de-intercalation.^[59] An additional peak is observed at 0.67 V in the first anodic sweep, which is commonly attributed to the SEI formation.^[59] The CV profile for OLC (Figure 3b), is quite similar to what has been reported previously.^[60] No sharp signals are observed in the voltage window suggesting gradual lithiation/de-lithiation in the material. There is a broad peak around 0.5 V in the first anodic sweep only. Dong et al. suggested that this peak is a result of increased electrolyte decomposition^[60] and subsequent SEI formation, likely due to the high active surface of the OLC material. Additional broad features are found in the anodic part at $1.25 \text{ V} \geq U \geq 0.6 \text{ V}$, partly superimposed by the SEI formation in the first cycle, and in the cathodic part at $0.75 \text{ V} \leq U \leq 1.75 \text{ V}$. The broad signals are well-silhouetted against the baseline and are likely due to Faradaic contributions of either the iron

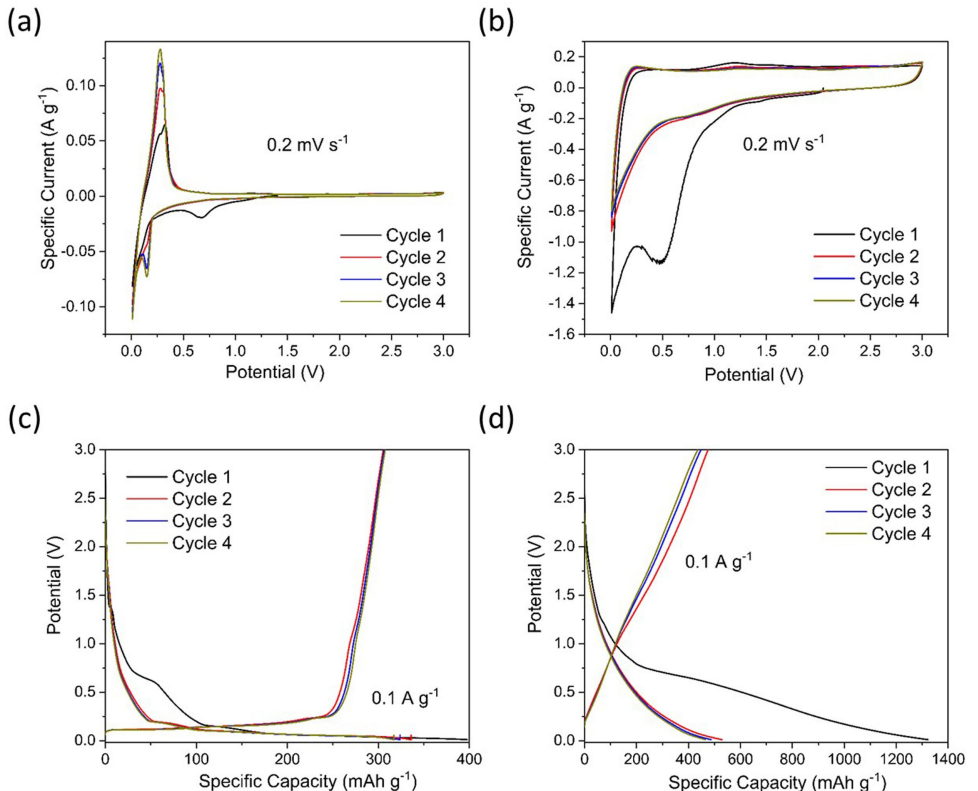


Figure 3. CV profiles of initial cycles, for a) graphite and b) OLC, GCPL profiles, potential vs. capacity, of initial cycles for c) graphite and d) OLC in LIB half-cell system (vs. Li/Li⁺).

compounds or oxygen-containing surface groups.^[61,62] Latter would be considered as most reasonable, as the remnant Fe-species are not directly accessible. The peak height decreases with further cycling which corresponds to a reaction of these groups possibly due to deactivation or removal.

Galvanostatic cycling under potential limitation (GCPL) was performed on the materials vs. Li/Li⁺. Figure 3c and d displays the voltage-capacity plots for the first four GCPL cycles at 0.1 A g⁻¹ (~0.3C rate considering theoretical capacity of graphite 372 mAh g⁻¹). Graphite (Figure 3c) showed regular lithiation/de-lithiation plateaus with significant capacity contribution at $U < 0.2$ V, consistent with the CV data. A small plateau-like event was recognized for the first discharge around 0.7 V, likely due to the SEI formation, corresponding to an initial irreversible capacity. A reversible capacity of around 325 mAh g⁻¹ was estimated for graphite electrodes in the next cycles. Similar to graphite, but a much-extended plateau at 0.7 V was seen for the OLC (Figure 3d). A very high irreversible capacity in the first cycle is seen for the OLC, which most likely results from an increased SEI formation due to a large surface area. Moreover, high surface area and high defect-density, as in the case for the OLC material, have both been reported to cause additional lithium entrapment contributing to a high initial irreversible capacity.^[63]

Starting with the second cycle, a gradual lithiation/de-lithiation profile was observed for the OLC electrodes which is in contrast to graphite. A similar lithiation/de-lithiation behavior has been reported in literature for other OLC materials.^[60] Such a sloping voltage profile is understood to be a result of a certain nanostructure, where the high surface area affects the site energy, decreasing the energy difference before and after lithiation.^[64] A high defect concentration in the OLC carbon, as seen in Raman measurements, may also contribute to such a feature.^[65] Moreover, the results of the N₂ physisorption experiments, described previously and shown in Figure S3, support the availability of the void inside the OLC shells. It is likely that there is a marked capacity contribution due to Li-ion storage inside the OLC shells, leading to ~500 mAh g⁻¹ reversible capacity in the initial cycles, significantly higher than the theoretical capacity of graphite.

The rate performance of graphite and OLC were evaluated in a current density variation from 0.1 to 10 A g⁻¹ and are shown in Figure 4a. A large irreversible capacity was observed for the OLC material in the initial cycles as discussed earlier. A higher specific capacity was observed at every current density for the OLC as compared to graphite. At 0.1 A g⁻¹, at the end of 10th cycle, a specific capacity of 307 mAh g⁻¹ and 395 mAh g⁻¹ was obtained for graphite and OLC, respectively. OLC performed remarkably well at high rates, and even at a very high current rate of 10 A g⁻¹, a stable capacity of 42 mAh g⁻¹ was obtained, in contrast to ~3 mAh g⁻¹ for graphite. High-rate cycling tests were also performed on the two materials. Figure 4b shows the cycling performance at 1 A g⁻¹ after initial formation cycles at 0.2 A g⁻¹. Both graphite and OLC show relatively stable cycling at 1 A g⁻¹, but graphite demonstrated a specific capacity of 104 mAh g⁻¹ at the end of 100 cycles, in contrast to 245 mAh g⁻¹ for the OLC. Although graphite showed a small recovery in specific capacity till 100th cycle, the OLC reached a capacity retention of 95.7% with respect to the 30th cycle at an average Coulombic efficiency of 99%. Thus, as compared to graphite, OLC delivers a superior electrochemical performance in LIB half-cells.

Understanding the charge storage dynamics in OLCs

In order to better understand the improved electrochemical performance of OLC, Electrochemical Impedance Spectroscopy (EIS) measurements were performed at the open circuit voltage (OCV) in half-cells before cycling and after 100 cycles for both graphite and OLC. The corresponding Nyquist plots are shown in Figure S4a and b. Two semi-circles are observed for cells after cycling due to SEI formation. The obtained data was subsequently fitted with equivalent circuit model (Figure S4c), and the results are summarized in Table S3. Before cycling, both graphite and OLC show a large charge transfer resistance R_{CT} . After cycling, the ionic pathways are established, so the R_{CT} is expected to decrease in general. Accordingly, the R_{CT} for both graphite and OLC is reduced. OLC shows a lower R_{CT} than graphite after 100 cycles, inferred to be a mark of a better Li-

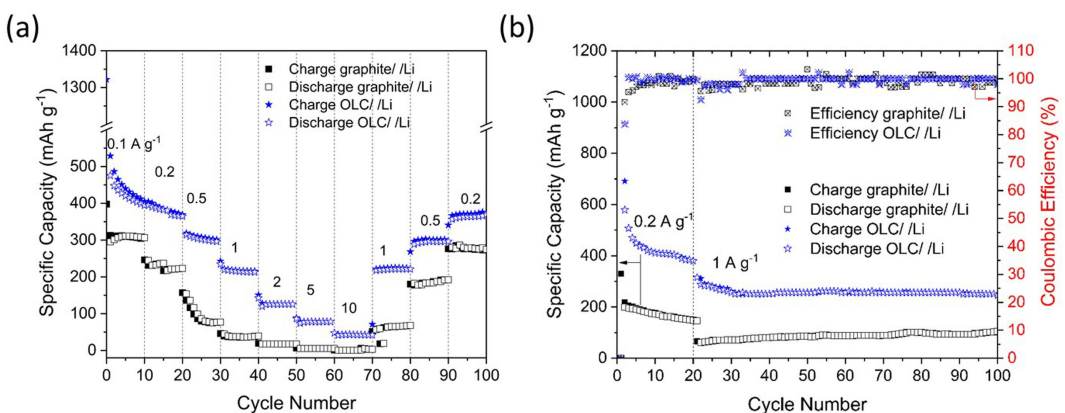


Figure 4. GCPL cycling for graphite and OLC in LIB half-cell system a) rate performance (current rates in the unit of A g⁻¹) and b) high-rate cycling.

transference. Regarding the SEI resistance, seen only in the data after cycling, the R_{SEI} is markedly larger for OLC as compared to graphite, in accordance with the aforementioned substantial SEI formation as a result of the significantly higher surface area.

For the purpose of elucidating the nature of the lithium intercalation in the OLC material, evaluation of diffusion and capacitive contributions to the overall capacity is important. Therefore, CV profiles at different scan rates (0.2–10 mV s⁻¹) were measured after a first formation cycle for both OLC and Graphite and are presented in Figure S5a and b. The peak intensity was analyzed with respect to the scan rate, and based on the power-law equation derived by Dunn's group for the calculation of pseudocapacitive contribution,^[66] the response characteristic of graphite and OLC in LIB half-cell system is evaluated, and the details of the calculations are given in the supplement.

The contributions of capacitive-controlled and diffusion-controlled capacity for each scan rate are calculated and are summarized in Figure 5a. Graphite appeared to have 8% capacitive contribution at the lowest scan rate, 0.2 mV s⁻¹, and gradually increasing as the scan rate rising until 29% at 10 mV s⁻¹. Higher capacitive contribution was possessed by OLC as it shows 21% at 0.2 mV s⁻¹, and superior than graphite at every scan rate reaching 64% at 10 mV s⁻¹. As expected, graphite has mostly diffusion-controlled capacity due to the lithium intercalation process, and low porosity. On the other hand, OLC shows much higher capacitive contribution indicating pseudocapacitive behavior. Mappings of the capacitive contributions of graphite and OLC at 1 mV s⁻¹ are presented in Figure S5c and S5d, respectively. It has been reported that the porosity and hierarchical morphology of a material could contribute to the pseudocapacitance/charge transfer,^[67] resulting in faster redox reaction and rate-independent characteristic during lithium intercalation.^[68] Moreover, an additional void volume is understood to be beneficial towards enhanced LIB^[69] and supercapacitor^[70] performance, and has also been reported for porous carbon materials.^[71]

Thus, in the half-cell LIB system, the OLC offers much higher specific capacity due to the charge storage contribution via the

EDLC process due to the high and electrochemically active surface area. In particular, this behavior further benefits from the accessible inner surface of the void^[72] as well as possible charge storage at defect-sites which has been described previously and was reported earlier. Figure 5 shows a schematic of the charge storage in the OLC structure aided particularly by the accessible inner mesoporous void via micropores in the shells. Additional nanopores due to distribution of OLC particles may also aid in the capacitive contribution to charge storage.^[73] At high currents, the capacity contributions from the diffusion-controlled graphitic part is systematically affected for both, the graphite and the OLC. However, in the OLC, the much smaller defect-rich graphitic domains improve the charge transfer and enable faster kinetics,^[74] which is further supported by the larger EDLC contributions, leading to a higher electrochemical performance. Therefore, it is highly promising to evaluate the OLC material for LIC application.

For a LIC, while the anode material is expected to deliver the highest capacity as possible while maintaining its stability, the cathode material requires a good capacitive behavior. The commercial activated carbon YP50F was selected as the cathode material. The AC was evaluated in a symmetric supercapacitor system and the CV data is plotted in Figure S6a. The CV exhibits a nearly rectangular shape even at various scan rates, indicating an ideal EDLC behavior and a fast electrochemical response.^[75] The specific capacitance at various current densities was recorded and was plotted in Figure S6b. The YP50F gives a good capacitive response until 5 A g⁻¹. In order to estimate the specific capacity for capacity balancing in LIC,^[76] AC was also evaluated in a half-cell LIB system (Figure S6c).

Electrochemical performance in LIC

For the full-cell LIC system, graphite or OLC were taken as the anode and AC was taken as the cathode. Accordingly, the corresponding LIC cells are henceforth referred to as graphite//AC and OLC//AC. The anode was pre-lithiated by the direct contact short-circuiting method, which also took into account

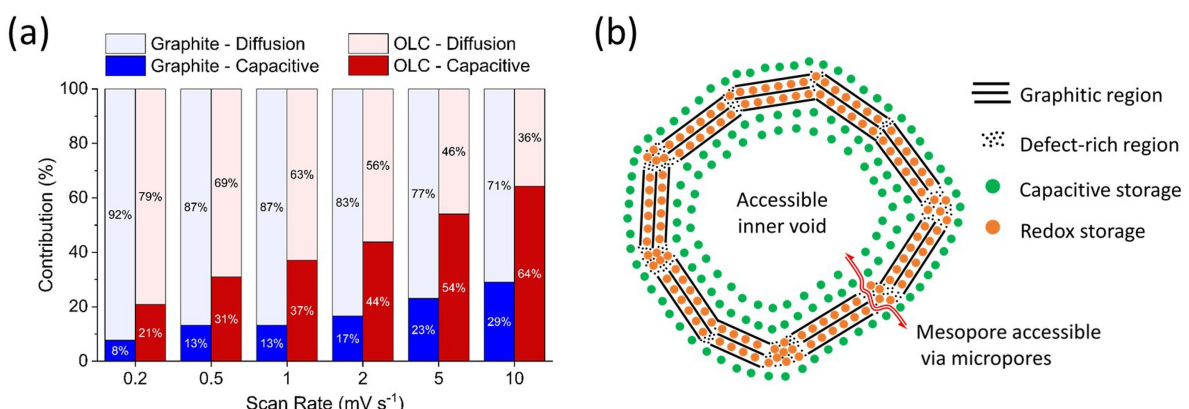


Figure 5. a) Capacitive-controlled and diffusion-controlled contributions to the capacity for graphite and OLC at different scan rates. b) Schematic of the charge storage mechanisms in OLC.

the large irreversible capacity due to SEI formation in the initial discharge cycle. Although alternative, more effective, pre-lithiation strategies have been discussed in literature,^[77] e.g., pre-lithiation in half-cells vs. Li with few cycles at low current rate, pre-lithiation mainly has a strong effect on the long-term cycling. Therefore, towards a more time-efficient processing, most of the electrochemical evaluation was done with direct contact pre-lithiation method, where the pre-lithiation time was minimized to only 1.5 h. The electrochemical measurements for the LIC system were conducted in a potential window of $2.2 \text{ V} \leq U \leq 3.8 \text{ V}$ as suggested for the working potential of a commercial LIC.^[78] Figure 6a and b shows the CV profiles for the graphite//AC and the OLC//AC cell, respectively. Both were measured at scan rates from 0.2 to 10 mV s⁻¹. The graphite//AC cell displayed a symmetrical supercapacitor-like profile with almost rectangular shape. However, for the OLC//AC cell, an asymmetrical profile was recorded. A larger area was located at the higher voltage region starting at 2.9 V. The phenomenon was particularly enhanced at higher current rates. An asymmetric CV profile as observed for OLC//AC was also reported for LIC systems utilizing a fully reduced graphene oxide as anode, with a surface area of 277 m² g⁻¹,^[79] where the particular profile is understood to be an indication of a higher storage capability of the LIC. The nature of the CV profiles was maintained at different scan rates for both graphite//AC and OLC//AC, indicating high reversibility.

Galvanostatic cycling was performed for graphite//AC and OLC//AC full-cell LIC systems at current densities from 0.1 to 10 A g⁻¹ in order to evaluate the rate performance. The voltage-time profiles for graphite//AC and OLC//AC at different current rates are shown in Figure 6c and d respectively, and the

comparative cycling data is shown in Figure 6e. The voltage-time profiles reveal linear relationship during charge and discharge for both systems, highlighting good capacitive behavior. This result is again consistent with the CV measurements. The charge-discharge profiles for graphite//AC cell were characterized by an unsymmetrical shape whereas symmetric profiles were recorded at all current rates for OLC//AC. In comparison to the graphite//AC cells, OLC//AC demonstrate longer charging and discharging times at the same current rate denoting a higher specific capacitance for the OLC-LIC system. The difference becomes even more significant at higher current rates and suggests better rate capability for the OLC-LIC than the graphite-LIC system.

Accordingly, in the cycling data (Figure 6e), as compared to graphite//AC, OLC//AC delivered a higher specific capacitance at every recorded current rate. At a low current of 0.1 A g⁻¹, graphite//AC exhibited a specific capacitance of 152 F g⁻¹ whereas OLC//AC delivered a specific capacitance of 337 F g⁻¹, more than a 200% improvement. At a high current of 10 A g⁻¹ graphite//AC showed a significant drop in specific capacitance reaching only 87 F g⁻¹ in contrast to OLC//AC, which maintained a specific capacitance of 214 F g⁻¹ at the high current rate. Both graphite//AC and OLC//AC showed high average Coulombic efficiency of ~98% after the initial formation period. When the current rate was reduced back to 0.2 A g⁻¹ the specific capacitances recovered back to 147 F g⁻¹ and 287 F g⁻¹ for graphite//AC and OLC//AC, respectively. The results clearly demonstrate the superior rate capability of the OLC-LIC system.

Subsequently, long-term high rate cycling at 1 A g⁻¹ was performed for both graphite//AC and OLC//AC, preceded by an initial formation cycling for 10 cycles at 0.1 A g⁻¹. It should be

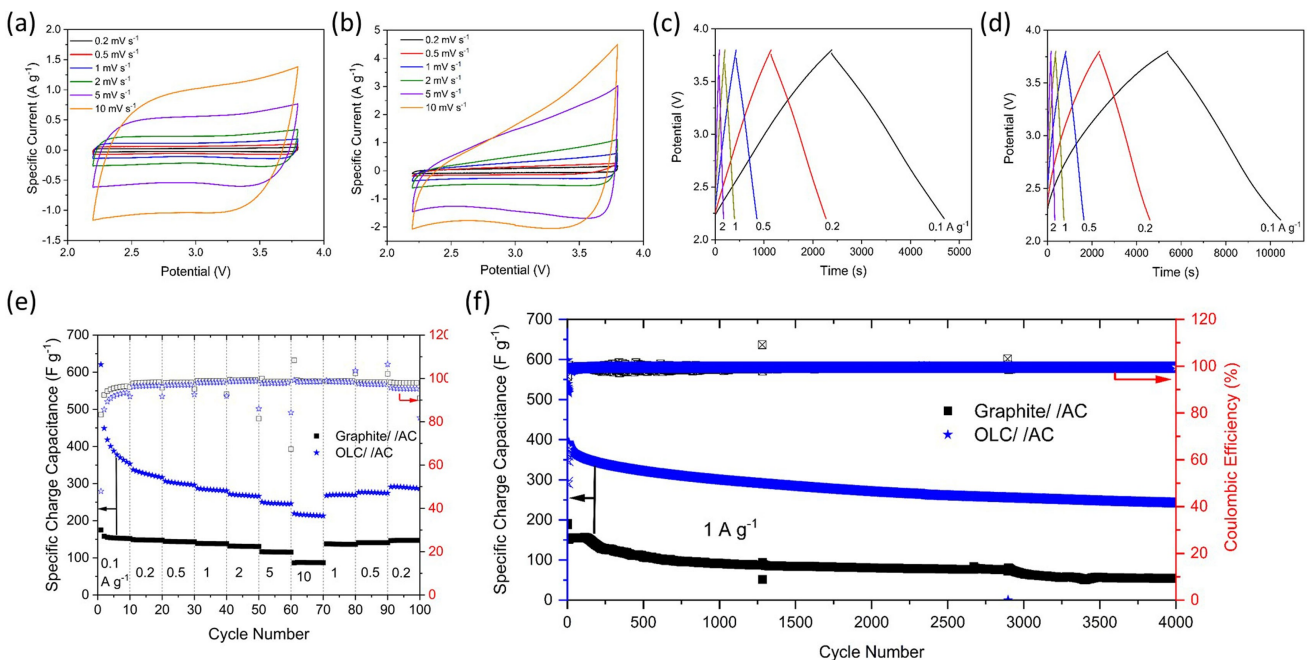


Figure 6. CV profiles at various scan rates of a) graphite//AC and b) OLC//AC. GCPL voltage vs. time profiles at various current densities for c) graphite//AC and d) OLC//AC. e) GCPL rate performance (current rates in the units of A g⁻¹), and f) long-term high-rate cycling performance at 1 A g⁻¹ in LIC system with slow pre-lithiation (normalized to the mass of active material in anode).

mentioned that for the long-term high-rate cycling, the Swagelok cells were found to be quite unsuitable, as shown in Figure S7a. For the LICs built in Swagelok cells with direct contact pre-lithiation, in addition to a strong fade in the capacitance retention for OLC//AC system, both graphite//AC and OLC//AC died after about 2500 cycles. This is likely due to inadequacies/variance with regards to pressure during manual sealing of the Swagelok cells and possible electrolyte losses due to excess free volume in the cells which become significant with long-term cycling.

Corresponding LICs built in coin cells with direct contact pre-lithiation, demonstrated significantly better cycling stability till 4000 cycles (Figure S7b). After the formation cycling, at 1 A g^{-1} graphite//AC showed a specific capacitance of 151 F g^{-1} whereas OLC//AC showed more than 2-fold higher specific capacitance of 355 F g^{-1} . After further 4000 cycles at 1 A g^{-1} , OLC//AC maintained a noticeably higher capacitance of 230 F g^{-1} as compared to graphite//AC with a specific capacitance of 75 F g^{-1} .

As mentioned earlier, pre-lithiation process may particularly affect long-term cycling. Hence, in order to better evaluate the long-term performance, LICs with slow cycling pre-lithiation process were prepared and investigated. The slow pre-lithiation of OLC and graphite involved 3 cycles at 0.1 A g^{-1} in a potential window of $0.01 \text{ V} \leq U \leq 3 \text{ V}$ (vs. Li/Li⁺), and were disassembled after the 4th lithiation half-cycle. As shown in Figure 6(f), slow pre-lithiated LICs showed a similar performance and stability as direct contact pre-lithiation (Figure S7b). After the formation cycling, at 1 A g^{-1} graphite//AC showed a specific capacitance of 152 F g^{-1} whereas OLC//AC showed a specific capacitance of 394 F g^{-1} . After further 4000 cycles at 1 A g^{-1} , slow pre-lithiated graphite//AC could only achieve a specific capacitance of 55 F g^{-1} , with a low capacitance retention of 36.1%, although at an average Coulombic efficiency of ~99.3%. In contrast, slow pre-lithiated OLC//AC retained a specific capacitance of 242 F g^{-1} , higher than in the case of direct contact pre-lithiation. The specific capacitance for OLC//AC after long-term cycling was more than 4 times higher as compared to slow pre-lithiated graphite//AC, accompanied by an 61.5% capacitance

retention, along with a highly stable average Coulombic efficiency of ~99.6%. Thus, the OLC-LIC system demonstrated significantly improved performance over the graphite-LIC system, with particular improvement in specific capacitance at higher rates, resulting from the superior morphology of OLCs.

Extended cycling was continued till 10,000 cycles for both direct-contact pre-lithiation and slow pre-lithiation coin cells and are given in Figure S8 of the supplement. Similar behavior as till 4000 cycles was observed for both OLC//AC and graphite//AC. Data for additional cells with slow pre-lithiation are also given due to technical issues during cycling. LICs with direct contact pre-lithiation exhibited capacitance fluctuations during cycling for both graphite//AC and OLC//AC, along with fluctuations in Coulombic efficiency. Nevertheless, slow pre-lithiation offered only a slight improvement in the specific capacitance as compared to direct contact pre-lithiation. Therefore, direct contact pre-lithiation being significantly more time and cost-efficient, would be more applicable for industrial implementation.

The performance of both the graphite//AC and OLC//AC LIC systems (in a potential window of $2.2 \text{ V} \leq U \leq 3.8 \text{ V}$) was summarized into a Ragone plot presented in Figure 7a by calculating the energy densities and power densities at various current densities, normalized to the mass of active material in both electrodes. Due to the high capacitive characteristics, the OLC//AC LIC system demonstrated a superior capability, reaching a maximum energy density of 195 Wh kg^{-1} at 138 W kg^{-1} power density and maximum power density of 17717 W kg^{-1} at 92 Wh kg^{-1} energy density in comparison to graphite//AC, which only reached a maximum energy density and power density of 112 Wh kg^{-1} at 174 Wh kg^{-1} and 17792 W kg^{-1} at 22 Wh kg^{-1} respectively.

Furthermore, we also conducted additional measurements for both LIC systems in the potential window of $2 \text{ V} \leq U \leq 4 \text{ V}$ as quite frequently this is also used in literature. Figure 7b shows the comparative Ragone plot for OLC//AC and graphite//AC in both potential windows along with some state-of-the-art LIC systems with carbonaceous anode materials evaluated in a potential window of $2 \text{ V} \leq U \leq 4 \text{ V}$ or wider (a detailed summary

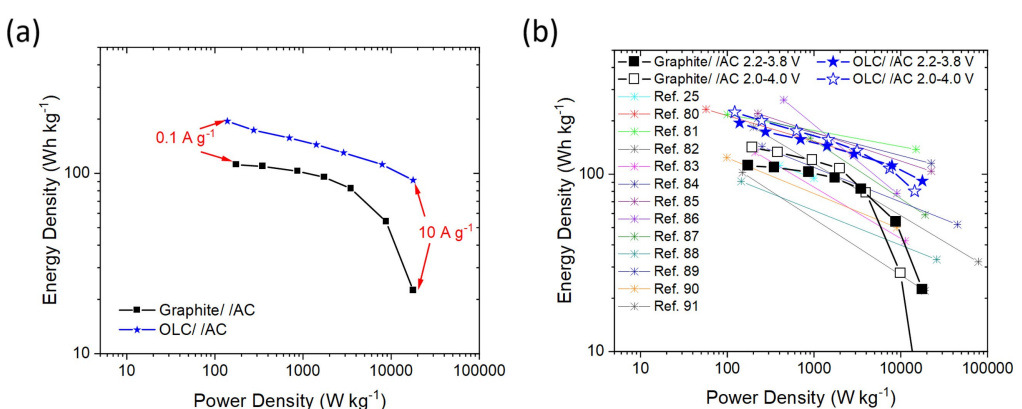


Figure 7. Ragone plot of graphite//AC and OLC//AC LIC cells a) in $2.2 \text{ V} \leq U \leq 3.8 \text{ V}$ potential window; the points correspond to energy and power density values at increasing current rates b) at different working potentials along with comparison to several LIC references with carbonaceous anode.^[25,80-91] (Normalized to the mass of active material in both electrodes). The values for references are summarized in Table S4.

is given in Table S4, including the mass loadings and cycle life). Graphite//AC could obtain a maximum energy density of 141 Wh kg^{-1} at 194 W kg^{-1} and reaching up to a maximum power density of 9938 W kg^{-1} at 28 Wh kg^{-1} for a current rate of 5 A g^{-1} . At a very high current rate of 10 A g^{-1} , graphite//AC cells showed negligible capacitance and therefore almost zero energy density. On the other hand, OLC//AC showed even better capability reaching a maximum energy density of 224 Wh kg^{-1} at a power density of 122 W kg^{-1} . OLC//AC showed considerable performance even at 10 A g^{-1} reaching a maximum power density of 14436 W kg^{-1} at 80 Wh kg^{-1} . The wider working voltage window further enhanced the electrochemical performance of both LIC systems up to a current density of 2 A g^{-1} . At higher current rates, the performance of graphite//AC was drastically affected, whereas OLC//AC only suffered from a small drop in energy density.

As shown in Figure 7b, our MOF-derived OLC-LIC demonstrated noticeably better performance than other graphite-based LICs reported in literature,^[25,92] particularly due to the significantly high surface area of the OLC prepared, and accordingly the obtained morphology, along with the improved Li-ion transfer. Our OLC-LIC system also shows better overall energy and power density values with longer cycle life than LICs with specialized carbonaceous anodes such as graphidyne, graphene etc.^[25,87,93] often evaluated with an even larger potential window (Table S4). Moreover, only a few reports exist for hybrid capacitors utilizing carbons with OLC-like features. OLC-like carbons prepared from sisal fiber as precursor for LICs were recently reported by Chen et al., although they do not classify them as OLC.^[25] In another recent work 2D–Ni-MOF-nanosheets were used as precursor to prepare OLC-like graphitic shells.^[92] However, the respective LICs demonstrated a maximum energy density of only 32 Wh kg^{-1} at 400 W kg^{-1} . The OLC-LIC presented herein outperforms the reported LICs based on OLC-like carbons, mainly due to the specialized morphology and high defect concentration enabling accessibility of inner voids.

The unique structure and morphology of the MOF-derived OLC material enabled excellent performance both in LIB half-cells and full-cell LIC systems. Thus, the rather straightforward synthesis route utilizing MOFs, not only yields high purity but also delivers highly advantageous structure and morphology of the OLC material, making it highly promising for industrial application.

Additionally, the MOF-route is particularly prospective towards further development of OLC material, as there is a possibility for significant variability in process parameters, such as system atmosphere and pressure, as well as through different precursor MOFs/additives, allowing for a large control of structure, morphology as well as dopants. The performance of OLC in LIB/LIC systems can therefore be further optimized.

Conclusion

OLC synthesized using an existing MOF-pyrolysis route was utilized as the anode material for LIC system paired with

commercial activated carbon. MOF-derived OLC exhibited remarkable properties of large surface area, high porosity, and large defect concentration. In comparison to graphite, the distinctive structure and morphology of OLC, leads to an exceptional electrochemical performance particularly at high rates, in both half-cell LIB and full-cell LIC systems. In LIB half-cells, OLC achieved a specific capacity of 395 mAh g^{-1} at 0.1 A g^{-1} and even at a high current of 10 A g^{-1} , showed a capacity of 42 mAh g^{-1} , whereas graphite could be barely cycled (3 mAh g^{-1}). LIC system with OLC anodes demonstrated superior specific capacitance and rate capability than with graphite until 10 A g^{-1} . Particularly in long-term high-rate cycling, OLC-LIC showed a highly stable Coulombic efficiency of $\sim 99.6\%$, such that even after 4000 cycles, more than 4-fold higher specific capacitance of 242 F g^{-1} was demonstrated in comparison to graphite-LIC. Moreover, OLC-LIC delivered exceptional energy density and power density reaching as high as 224 Wh kg^{-1} and 14436 W kg^{-1} respectively. The significantly better electrochemical performance of OLC-LIC as compared to graphite-LIC, particularly at high rates, clearly demonstrates the high potential of the MOF-derived OLC material towards practical LIC application. Moreover, the easy applicability of the synthesis process, may enable direct industrial implementation. There is also a wide scope of further developing the OLC material, through structure/morphology modifications, dopants and surface functionalization/activation, towards various energy storage systems.

Experimental Section

Materials

Basolite F300 (CAS: 1195763-37-1) was obtained from Sigma Aldrich and used as received. Fuming hydrochloric acid (HCl, 37%) from Merck KGaA and ethanol (99%) from Berkel AHK were used. Battery grade graphite KS6 L and conductive carbon black (Super C65) were purchased from Imerys. Activated carbon YP50F was obtained from Kuraray Chemical. Co., Japan. Polyvinylidene difluoride (PVDF) powder Solef® 1013 was purchased from Solvay Solexis, Inc. N-methyl-2-pyrrolidone (NMP) was obtained from Sigma Aldrich. Copper foil with a thickness of $9 \mu\text{m}$ from MTI Corp. and aluminum foil from OTMT, U.K., with a thickness of $15 \mu\text{m}$ were used as current collectors without any treatment.

Synthesis of OLC

OLC was prepared according to a previous work.^[29] For the synthesis of the OLCs, 1 g of Basolite F300 was filled in an alumina combustion boat which was then placed in a Nabertherm tube furnace. Under a steady flow of argon gas at 0.15 L min^{-1} , a heating rate of $5 \text{ }^{\circ}\text{C min}^{-1}$ was applied until $800 \text{ }^{\circ}\text{C}$. After a temperature dwell time of 1 h, the system was allowed to cool down overnight. Samples were removed from the furnace, ground, and stirred in a solution of HCl and ethanol (3:1 v/v) overnight to etch the obtained iron compounds. The solution was then washed by 600 mL ethanol and 200 mL H_2O via centrifugation and finished by vacuum filtration. After overnight drying in an oven at $80 \text{ }^{\circ}\text{C}$, the powder sample is ground and subsequently used for characterization and electrode preparation. With an ICP-OES analysis an iron residual of 0.31 wt.% was determined in the as-prepared material.

After a subsequent grinding step, the powder was used for further characterization and electrode preparation.

Electrode preparation

The anode slurry was made by mixing 1 g OLC with carbon black (Super C65) as a conductive agent and PVDF as a binder, in a weight ratio of 85:5:10, respectively, dispersed in 10 mL NMP. The slurry was mixed with a Retsch MM200 shaker mill for 30 min at 25 Hz. The prepared slurry was coated onto the copper foil by the doctor blade coating method with a blade height of 250 μm , using an Erichsen Coatmaster 509 film applicator and a Zehntner ZUA 2000 blade. The coating was dried in an oven at 80 °C for 24 h, then punched into electrodes of 12 mm in diameter and then vacuum dried at 80 °C for over 8 h. Electrodes with the graphite KS6 L were prepared with the same additive composition and coating process. The average mass loading was $\sim 0.6 \text{ mg cm}^{-2}$ for graphite anode and $\sim 0.4 \text{ mg cm}^{-2}$ for OLC anode.

For the cathode slurry, 1 g activated carbon YP50F was mixed with Super C65 and PVDF in a weight ratio of 70:10:20, dispersed in 6.5 mL NMP. After mixing with the shaker mill for 30 min at 25 Hz, the slurry was coated onto aluminum foil with a blade height of 250 μm . The average mass loading of the cathode was $\sim 2 \text{ mg cm}^{-2}$.

Characterization methods

Powder X-ray diffraction (XRD) experiments were conducted with a STOE (Darmstadt, Germany) STADI P diffractometer ($\text{Co } K_{\alpha 1}$ radiation, $\lambda = 1.78896 \text{ \AA}$, curved Ge(111) crystal Johann-type monochromator, Dectris single-strip Mythen 1 K detector) in transmission mode as flat samples glued between two acetate sheets.

Scanning electron microscopy (SEM) was carried out with a LEO Gemini 1530 microscope using 15 kV acceleration voltage. For high resolution transmission electron microscopy (HR-TEM), a FEI Tecnai F30 and a FEI-TITAN with a Cs-aberration correction system operated at 300 kV were used.

Raman spectroscopy was measured using a Thermo Scientific Smart DXR Raman spectrometer with an excitation laser wavelength of 532 nm, a laser power of 3 mW and a spot size of 2.1 μm . In order to evaluate the integrated intensities, the core level signals were fitted with a Gaussian function using a non-linear Shirley-type background.

The nitrogen sorption measurements were carried out using a Quantachrome Quadrasorb SI apparatus. Prior to the measurements, the samples were degassed under a dynamic vacuum at 150 °C for 8 h. Specific surface areas were calculated by the multi-point Brunauer-Emmet-Teller (BET) method using a relative pressure range of $0.05 \leq p/p_0 \leq 0.2$. The total pore volume was determined at $p/p_0 = 0.97$. The pore size distributions (PSDs) were calculated using the Quenched Solid Density Functional Theory (QSDFT) with N_2 -carbon equilibrium transition kernel at 77 K based on a slit-pore model.

X-ray photoelectron spectroscopy (XPS) was carried out on powder samples, using a PHI 5600 CI spectrometer (Physical Electronics Inc., Chanhassen, MN, USA) system with monochromatic Al K_{α} radiation (350 W) at a pass energy of 29 eV and a step size of 0.1 eV. The binding energy scale of the spectrometer was calibrated with Au metal foils for the binding energy (BE) of Au 4f_{7/2} at 84.0 eV and Cu foil for the BE of Cu 2p_{3/2} at 932.7 eV. All spectra were recorded in an energy range of 0–1000 eV with a hemispherical analyzer. The binding energies of the spectra were calibrated according to artificial carbon

contamination with the C 1s BE at 284.8 eV. Elemental concentrations from the XPS were calculated using standard single-element sensitivity factors. The selected spectra were fitted with Gaussian peak functions using a non-linear Shirley-type background.

Iron content in carbon materials was measured using inductively coupled plasma-optical emission spectrometry (ICP-OES) on an iCAP 6500 Duo View (Thermo Fisher Scientific, USA) at the three wavelengths 240.488, 259.837, and 259.940 nm.

Electrochemical measurements

All electrochemical measurements were performed in 2-electrode Swagelok cells, unless otherwise stated. The cells were built inside an MBraun glovebox, ensuring H_2O and O_2 contents stay below 0.1 ppm. All measurements were conducted at 25 °C in a temperature chamber. Celgard 2500 was used as the separator. LP30 (1 M LiPF₆ in 1:1 (v/v) mixture of ethylene carbonate and dimethyl carbonate) was purchased from BASF and used as the electrolyte.

Half-cells for LIB testing were built with electrochemical grade lithium chips (Chempur, 250 μm thickness) as the counter electrode. For the full-cell LIC assembly, anodes were pre-lithiated by a direct contact with the lithium foil, based on a literature procedure.^[94] Sufficient LP30 electrolyte was first used to wet all the contact area of electrode and Li foil, which were then pressed between two glass substrates and held with binder clips for 1.5 h. After the pre-lithiation process, the electrodes were separated, and immediately taken for full-cell assembly. LIC full-cells were assembled with the pre-lithiated OLC or graphite as anode and activated carbon as cathode. All the prepared cells were rested for 18 h to ensure a good contact of the electrolyte with the electrodes and the separator before the electrochemical measurements.

All the electrochemical measurements were performed in a Biologic VMP3 (France) multichannel potentiostat. Galvanostatic cycling with potential limitation (G CPL) was carried out at different current rates. For the half-cell LIB tests, a voltage window of $0.01 \leq U \leq 3 \text{ V}$ (vs. Li/Li⁺) was used for OLC and graphite. In order to evaluate the corresponding capacity of activated carbon for full-cell balancing, an appropriate window of $2 \leq U \leq 4 \text{ V}$ (vs. Li/Li⁺) was used. Meanwhile for full-cell LICs, voltage windows of $2.2 \leq U \leq 3.8 \text{ V}$ and $2 \leq U \leq 4 \text{ V}$ were applied. Cyclic voltammetry (CV) was conducted with scan rates varying from 0.2 to 10 mV s^{-1} .

Electrochemical impedance spectroscopy (EIS) measurements were carried out in the frequency range of 200 kHz to 100 mHz using an AC voltage amplitude of 5 mV. The simulation of the electric equivalent circuit model and the fitting of the EIS spectra were carried out using the Relaxis3 software from rhd instruments GmbH & Co. KG.

The details of the calculations for specific capacity and specific capacitance along with that for energy density and power density of the LIC are given in the Section 1 and 2 of the Supporting Information, respectively. Additionally, explanation of the calculation performed for the capacitive- and diffusion-controlled contributions to charge storage are given in Section 3 of the supplement. The energy density and power density were calculated based on the total mass of the active material of both electrodes.

Acknowledgements

A.D.C.P. would like to thank the Deutscher Akademischer Austauschdienst (DAAD) for doctoral grant. A.O. would like to acknowledge the financial support from the Federal Ministry of

Education and Research (BMBF) under grant no. 03XP0254D (Cluster of Competence for Battery Materials ExcellMatBat: KaSiLi project). The authors would like to thank A. Voß (IFW Dresden) for the ICP measurements and S. Kaschube (IFW Dresden) for help with the XPS measurements. Open Access funding enabled and organized by Projekt DEAL.

Conflict of Interest

The authors declare no conflict of interest.

Data Availability Statement

The data that support the findings of this study are available from the corresponding author upon reasonable request.

Keywords: anode · high energy density · high power density · Li-ion capacitors · onion-like carbons

- [1] W. Zuo, R. Li, C. Zhou, Y. Li, J. Xia, J. Liu, *Adv. Sci.* **2017**, *4*, 1600539.
- [2] K. Naoi, Y. Nagano, *Li-Ion-Based Hybrid Supercapacitors in Organic Medium*, Wiley-VCH Verlag GmbH & Co. KGaA, Weinheim, Germany, **2013**.
- [3] A. M. Bittner, M. Zhu, Y. Yang, H. F. Waibel, M. Konuma, U. Starke, C. J. Weber, *J. Power Sources* **2012**, *203*, 262–273.
- [4] S. Ban, J. Zhang, L. Zhang, K. Tsay, D. Song, X. Zou, *Electrochim. Acta* **2013**, *90*, 542–549.
- [5] J. Asenbauer, T. Eisenmann, M. Kuenzel, A. Kazzazi, Z. Chen, D. Bresser, *Sustain. Energy Fuels* **2020**, *4*, 5387–5416.
- [6] P. Bai, J. Guo, M. Wang, A. Kushima, L. Su, J. Li, F. R. Brushett, M. Z. Bazant, *Joule* **2018**, *2*, 2434–2449.
- [7] L. S. Roselin, R.-S. Juang, C.-T. Hsieh, S. Sagadevan, A. Umar, R. Selvin, H. H. Hegazy, *Materials* **2019**, *12*, 1229.
- [8] E. G. Leggesse, C.-L. Chen, J.-C. Jiang, *Carbon* **2016**, *103*, 209–216.
- [9] A. Vu, Y. Qian, A. Stein, *Adv. Energy Mater.* **2012**, *2*, 1056–1085.
- [10] J. Bartelmess, S. Giordani, *Beilstein J. Nanotechnol.* **2014**, *5*, 1980–1998.
- [11] C. N. R. Rao, R. Seshadri, A. Govindaraj, R. Sen, *Mater. Sci. Eng. R Rep.* **1995**, *15*, 209–262.
- [12] M. Zeiger, N. Jäckel, V. N. Mochalin, V. Presser, *J. Mater. Chem. A* **2016**, *4*, 3172–3196.
- [13] I. Y. Y. Bu, *Sol. Energy* **2014**, *105*, 236–242.
- [14] J. K. McDonough, A. I. Frolov, V. Presser, J. Niu, C. H. Miller, T. Ubieto, M. V. Fedorov, Y. Gogotsi, *Carbon* **2012**, *50*, 3298–3309.
- [15] G. Wu, C. Dai, D. Wang, D. Li, N. Li, *J. Mater. Chem.* **2010**, *20*, 3059–3068.
- [16] D. Han, H. Hu, B. Liu, G. Song, H. Yan, J. Di, *Ceram. Int.* **2016**, *42*, 12460–12466.
- [17] C. Zhang, J. Li, E. Liu, C. He, C. Shi, X. Du, R. H. Hauge, N. Zhao, *Carbon* **2012**, *50*, 3513–3521.
- [18] D. Pech, M. Brunet, H. Durou, P. Huang, V. Mochalin, Y. Gogotsi, P.-L. Taberna, P. Simon, *Nat. Nanotechnol.* **2010**, *5*, 651–654.
- [19] S. Fleischmann, N. Jäckel, M. Zeiger, B. Krüner, I. Grobelsk, P. Formanek, S. Choudhury, D. Weingarth, V. Presser, *Chem. Mater.* **2016**, *28*, 2802–2813.
- [20] S. Fleischmann, A. Tolosa, M. Zeiger, B. Krüner, N. J. Peter, I. Grobelsk, A. Quade, A. Kruth, V. Presser, *J. Mater. Chem. A* **2017**, *5*, 2792–2801.
- [21] S. Fleischmann, M. Zeiger, N. Jäckel, B. Krüner, V. Lemkova, M. Widmaier, V. Presser, *J. Mater. Chem. A* **2017**, *5*, 13039–13051.
- [22] N. Sano, H. Wang, I. Alexandrou, M. Chhowalla, K. B. K. Teo, G. A. J. Amaralunga, K. Iimura, *J. Appl. Phys.* **2002**, *92*, 2783–2788.
- [23] R. Borgohain, J. Yang, J. P. Selegue, D. Y. Kim, *Carbon* **2014**, *66*, 272–284.
- [24] H. Jin, S. Wu, T. Li, Y. Bai, X. Wang, H. Zhang, H. Xu, C. Kong, H. Wang, *Appl. Surf. Sci.* **2019**, *488*, 593–599.
- [25] Z. Yang, H. Guo, X. Li, Z. Wang, J. Wang, Y. Wang, Z. Yan, D. Zhang, *J. Mater. Chem. A* **2017**, *5*, 15302–15309.
- [26] J. Chen, B. Yang, H. Li, P. Ma, J. Lang, X. Yan, *J. Mater. Chem. A* **2019**, *7*, 9247–9252.
- [27] R. R. Salunkhe, Y. V. Kaneti, J. Kim, J. H. Kim, Y. Yamauchi, *Acc. Chem. Res.* **2016**, *49*, 2796–2806.
- [28] B. Xu, H. Zhang, H. Mei, D. Sun, *Coord. Chem. Rev.* **2020**, *420*, 213438.
- [29] M. Klose, K. Pinkert, M. Zier, M. Uhlemann, F. Wolke, T. Jaumann, P. Jehnichen, D. Wadezitz, S. Oswald, J. Eckert, L. Giebel, *Carbon* **2014**, *79*, 302–309.
- [30] G. Moussa, C. Matei Ghime, P.-L. Taberna, P. Simon, C. Vix-Guterl, *Carbon* **2016**, *105*, 628–637.
- [31] G. Carotenuto, S. De Nicola, M. Palomba, D. Pullini, A. Horsewell, T. W. Hansen, L. Nicolais, *Nanotechnology* **2012**, *23*, 485705.
- [32] P. Delhaes, *Graphite and precursors*, Vol. 1, CRC Press, Boca Raton, **2000**.
- [33] P. Trucano, R. Chen, *Nature* **1975**, *258*, 136–137.
- [34] H. Lipson, A. R. Stokes, *Nature* **1942**, *149*, 328–328.
- [35] M. Bystrzejewski, M. H. Rummeli, T. Gemming, H. Lange, A. Huczko, *New. Carbon. Mater.* **2010**, *25*, 1–8.
- [36] Y. Gogotsi, V. Presser, *Carbon nanomaterials*, CRC Press, Boca Raton, **2013**.
- [37] N. Jäckel, D. Weingarth, A. Schreiber, B. Krüner, M. Zeiger, A. Tolosa, M. Aslan, V. Presser, *Electrochim. Acta* **2016**, *191*, 284–298.
- [38] L. G. Cançado, A. Jorio, E. H. M. Ferreira, F. Stavale, C. A. Achete, R. B. Capaz, M. V. O. Moutinho, A. Lombardo, T. S. Kulmala, A. C. Ferrari, *Nano Lett.* **2011**, *11*, 3190–3196.
- [39] M. S. Dresselhaus, G. Dresselhaus, A. Jorio, A. G. Souza Filho, R. Saito, *Carbon* **2002**, *40*, 2043–2061.
- [40] K. N. Kudin, B. Ozbas, H. C. Schniepp, R. K. Prud'homme, I. A. Aksay, R. Car, *Nano Lett.* **2008**, *8*, 36–41.
- [41] A. C. Ferrari, J. Robertson, *Phys. Rev. B* **2000**, *61*, 14095–14107.
- [42] V. Zólyomi, J. Koltai, J. Kürti, *Phys. Status Solidi B* **2011**, *248*, 2435–2444.
- [43] Z. Ma, Y. Zhuang, Y. Deng, X. Song, X. Zuo, X. Xiao, J. Nan, *J. Power Sources* **2018**, *376*, 91–99.
- [44] J. F. Moulder, J. Chastain, *Handbook of X-ray Photoelectron Spectroscopy: A Reference Book of Standard Spectra for Identification and Interpretation of XPS Data*, Physical Electronics Division, Perkin-Elmer Corporation, **1992**.
- [45] G. Panzner, W. Diekmann, *Surf. Sci.* **1985**, *160*, 253–270.
- [46] H. J. Grabke, *ISIJ Int.* **1989**, *29*, 529–538.
- [47] H. P. Bonzel, H. J. Krebs, *Surf. Sci.* **1980**, *91*, 499–513.
- [48] A. Furlan, U. Jansson, J. Lu, L. Hultman, M. Magnuson, *J. Phys. Condens. Matter* **2015**, *27*, 045002.
- [49] Z. Yang, T. Zhao, X. Huang, X. Chu, T. Tang, Y. Ju, Q. Wang, Y. Hou, S. Gao, *Chem. Sci.* **2017**, *8*, 473–481.
- [50] Z. Tian, C. Wang, J. Yue, X. Zhang, L. Ma, *Catal. Sci. Technol.* **2019**, *9*, 2728–2741.
- [51] M. Thommes, K. Kaneko, A. Neimark, J. Olivier, F. Rodriguez-Reinoso, J. Rouquerol, K. Sing, *Pure Appl. Chem.* **2015**, *87*, 1051–1069.
- [52] M. Klose, R. Reinhold, K. Pinkert, M. Uhlemann, F. Wolke, J. Balach, T. Jaumann, U. Stoeck, J. Eckert, L. Giebel, *Carbon* **2016**, *106*, 306–313.
- [53] P.-J. Yen, S. K. Sahoo, Y.-C. Chiang, S.-Y. Huang, C.-W. Wu, Y.-C. Hsu, K.-H. Wei, *Nanoscale Res. Lett.* **2019**, *14*, 141.
- [54] Q. Wu, J. Liang, J.-D. Yi, D.-L. Meng, P.-C. Shi, Y.-B. Huang, R. Cao, *Dalton Trans.* **2019**, *48*, 7211–7217.
- [55] M. Thommes, *Chem. Ing. Tech.* **2010**, *82*, 1059–1073.
- [56] Y. Zeng, C. Fan, D. D. Do, D. Nicholson, *Ind. Eng. Chem. Res.* **2014**, *53*, 15467–15474.
- [57] M. A. B. Alatmirano, S. Cordero, G. Román, A. G. Goicochea, *Adsorpt. Sci. Technol.* **2015**, *33*, 307–319.
- [58] P. T. M. Nguyen, C. Fan, D. D. Do, D. Nicholson, *J. Phys. Chem. C* **2013**, *117*, 5475–5484.
- [59] B. Xing, C. Zhang, Y. Cao, G. Huang, Q. Liu, C. Zhang, Z. Chen, G. Yi, L. Chen, *Fuel Process. Technol.* **2018**, *172*, 162–171.
- [60] J. Dong, T. Zhang, D. Zhang, W. Zhang, H. Zhang, R. Liu, M. Yao, B. Liu, *Nanotechnology* **2016**, *28*, 035704.
- [61] M. B. Sassin, A. N. Mansour, K. A. Pettigrew, D. R. Rolison, J. W. Long, *ACS Nano* **2010**, *4*, 4505–4514.
- [62] M. Seredych, D. Hulicova-Jurcakova, G. Q. Lu, T. J. Bandosz, *Carbon* **2008**, *46*, 1475–1488.
- [63] K. Omichi, G. Ramos-Sánchez, R. Rao, N. Pierce, G. Chen, P. B. Balbuena, A. R. Harutyunyan, *J. Electrochem. Soc.* **2015**, *162*, A2106-A2115.
- [64] C. Liu, Z. G. Neale, G. Cao, *Mater. Today* **2016**, *19*, 109–123.
- [65] A. Shellikeri, V. Watson, D. Adams, E. E. Kalu, J. A. Read, T. R. Jow, J. S. Zheng, J. P. Zheng, *J. Electrochem. Soc.* **2017**, *164*, A3914-A3924.
- [66] J. Wang, J. Polleux, J. Lim, B. Dunn, *J. Phys. Chem. C* **2007**, *111*, 14925–14931.

- [67] T. Brezesinski, J. Wang, S. H. Tolbert, B. Dunn, *Nat. Mater.* **2010**, *9*, 146–151.
- [68] Y. Lan, H. Zhao, Y. Zong, X. Li, Y. Sun, J. Feng, Y. Wang, X. Zheng, Y. Du, *Nanoscale* **2018**, *10*, 11775–11781.
- [69] Y. Xiang, Z. Yang, S. Wang, M. S. A. Hossain, J. Yu, N. A. Kumar, Y. Yamauchi, *Nanoscale* **2018**, *10*, 18010–18018.
- [70] J. Shao, X. Zhou, Q. Liu, R. Zou, W. Li, J. Yang, J. Hu, *J. Mater. Chem. A* **2015**, *3*, 6168–6176.
- [71] J. Niu, R. Shao, M. Liu, J. Liang, Z. Zhang, M. Dou, Y. Huang, F. Wang, *Energy Storage Mater.* **2018**, *12*, 145–152.
- [72] E. J. Lee, L. Lee, M. A. Abbas, J. H. Bang, *Phys. Chem. Chem. Phys.* **2017**, *19*, 21140–21151.
- [73] W. Zhang, J. Wang, L. Bao, Z. Gao, J. Yu, *Diamond Relat. Mater.* **2019**, *96*, 231–236.
- [74] D. Zhang, G. Wang, L. Xu, J. Lian, J. Bao, Y. Zhao, J. Qiu, H. Li, *Appl. Surf. Sci.* **2018**, *451*, 298–305.
- [75] X. Gao, C. Zhan, X. Yu, Q. Liang, R. Lv, G. Gai, W. Shen, F. Kang, Z.-H. Huang, *Materials* **2017**, *10*, 414.
- [76] X. Sun, X. Zhang, W. Liu, K. Wang, C. Li, Z. Li, Y. Ma, *Electrochim. Acta* **2017**, 235.
- [77] M. Arnaiz, J. Ajuria, *Batteries & Supercaps* **2021**, *4*, 733–748.
- [78] A. Sato, *TAIYO YUDEN Lithium Ion Capacitors: An Effective EDLC Replacement (white paper)*, Taiyo Yuden.
- [79] T. Zhang, F. Zhang, L. Zhang, Y. Lu, Y. Zhang, X. Yang, Y. Ma, Y. Huang, *Carbon* **2015**, *92*, 106–118.
- [80] W. Ahn, D. U. Lee, G. Li, K. Feng, X. Wang, A. Yu, G. Lui, Z. Chen, *ACS Appl. Mater. Interfaces* **2016**, *8*, 25297–25305.
- [81] K. Wang, N. Wang, J. He, Z. Yang, X. Shen, C. Huang, *Electrochim. Acta* **2017**, 253, 506–516.
- [82] J. Ajuria, E. Redondo, M. Arnaiz, R. Mysyk, T. Rojo, E. Goikolea, *J. Power Sources* **2017**, *359*, 17–26.
- [83] W. S. V. Lee, X. Huang, T. L. Tan, J. M. Xue, *ACS Appl. Mater. Interfaces* **2018**, *10*, 1690–1700.
- [84] F. Sun, X. Liu, H. B. Wu, L. Wang, J. Gao, H. Li, Y. Lu, *Nano Lett.* **2018**, *18*, 3368–3376.
- [85] Q. Xia, H. Yang, M. Wang, M. Yang, Q. Guo, L. Wan, H. Xia, Y. Yu, *Adv. Energy Mater.* **2017**, *7*, 1701336.
- [86] D. P. Dubal, P. Gomez-Romero, *Mater. Today* **2018**, *8*, 109–117.
- [87] X.-Y. Shan, Y. Wang, D.-W. Wang, F. Li, H.-M. Cheng, *Adv. Energy Mater.* **2016**, *6*, 1502064.
- [88] G. Moreno-Fernández, M. Granados-Moreno, J. L. Gómez-Urbano, D. Carriazo, *Batteries & Supercaps* **2021**, *4*, 469–478.
- [89] M. Chen, T. Le, Y. Zhou, F. Kang, Y. Yang, *ACS Sustain. Chem. Eng.* **2021**, *9*, 10054–10061.
- [90] Y. An, C. Li, X. Sun, K. Wang, F. Su, F. Liu, X. Zhang, Y. Ma, *J. Phys. D* **2021**, *55*, 045501.
- [91] M. Liu, Z. Zhang, M. Dou, Z. Li, F. Wang, *Carbon* **2019**, *151*, 28–35.
- [92] K. Wang, Z. Wang, J. Liu, C. Li, F. Mao, H. Wu, Q. Zhang, *ACS Appl. Mater. Interfaces* **2020**, *12*, 47482–47489.
- [93] X. Han, P. Han, J. Yao, S. Zhang, X. Cao, J. Xiong, J. Zhang, G. Cui, *Electrochim. Acta* **2016**, *196*, 603–610.
- [94] M. Kim, F. Xu, J. H. Lee, C. Jung, S. M. Hong, Q. M. Zhang, C. M. Koo, *J. Mater. Chem. A* **2014**, *2*, 10029–10033.

Manuscript received: November 19, 2021

Revised manuscript received: January 21, 2022

Version of record online: February 21, 2022